Science Advances
AAAS

# Supplementary Materials for

## Leaping liquid crystal elastomers

Tayler S. Hebner *et al.*

Corresponding author: Timothy J. White, timothy.j.white@colorado.edu

*Sci. Adv.* **9**, eade1320 (2023)
DOI: 10.1126/sciadv.ade1320

**The PDF file includes:**



**Other Supplementary Material for this manuscript includes the following:**

**Supplementary Text**

Outline of Computational Method

We modeled the transient behavior of the sheet up until the point of snap-through. During this period, the sheet deformed slowly in response to changes in temperature distribution and therefore inertial effects are negligible. Further, heat transfer is slow compared to mechanical time scales, and therefore it was assumed that the body is in mechanical equilibrium at each instant of time. The temperature profile was obtained by solving the heat equation assuming a set temperature on the bottom side and an insulated boundary on the top. The temperature distribution through the thickness gives rise to a spontaneous strain and curvature in the sheet. We obtain these values by imposing equilibrium (balance of force and moment) across the cross-section. Given the spontaneous strain and curvature, a Föppl-von Kármán plate model was used to calculate the equilibrium shape, and then the stability of the equilibrium shape was studied to determine the instant of snap-through.

Evolution of Strain

A plane state of stress in the sheet was assumed, and therefore the Hooke's law may be written as

$$\boldsymbol{\sigma^s_{\alpha\beta}(z) = \frac{E(z)}{1-\nu^2}\left(\nu\,\epsilon^s_{\gamma\gamma}(z)\delta_{\alpha\beta} + (1-\nu)\epsilon^s_{\alpha\beta}(z)\right) = E(z)f_{\alpha\beta\gamma\delta}\epsilon^s_{\alpha\beta}(z).}$$

where z is the variable through the thickness, the Young's modulus $E(z)$ varies through the thickness while the Poisson's relation $\nu$ is uniform. This allows Hooke's law to be written in the compact form of the second equality. The usual ansatz was made that the through-thickness strain takes the form

$$\epsilon^s_{\alpha\beta}(z) = \kappa_{\alpha\beta}(z - z_0) + \epsilon_{\alpha\beta} - \hat{\epsilon}_{\alpha\beta}(z)$$

where $\kappa_{\alpha\beta}$ is the apparent curvature, $z_0$ is the location of the neutral axis, $\epsilon_{\alpha\beta}$ is the in-plane strain, and $\hat{\epsilon}_{\alpha\beta}(z)$ is the spontaneous strain due to the local temperature profile. The traction can be written as

$$N_{\alpha\beta} = \int_{-\frac{h}{2}}^{\frac{h}{2}} \sigma^s_{\alpha\beta}(z)dz = \int_{-\frac{h}{2}}^{\frac{h}{2}} E(z)f_{\alpha\beta\gamma\delta}\left(\kappa_{\gamma\delta}(z - z_0) + \epsilon_{\gamma\delta} - \hat{\epsilon}_{\gamma\delta}(z)\right)dz$$
$$= f_{\alpha\beta\gamma\delta}(\kappa_{\gamma\delta}\left(\mathcal{M}^1(E) - z_0\mathcal{M}^0(E)\right) + \epsilon_{\gamma\delta}\mathcal{M}^0(E) - \mathcal{M}^0\left(E\,\hat{\epsilon}_{\gamma\delta}\right).$$

Setting $z_0 = \frac{\mathcal{M}^1(E)}{\mathcal{M}^0(E)}$, we get

$$N_{\alpha\beta} = C\, f_{\alpha\beta\gamma\delta}\left(\epsilon_{\gamma\delta} - \epsilon^m_{\gamma\delta}\right)$$

where the effective in-plane modulus is given by $C = \mathcal{M}^0(E)$ and the spontaneous effective in-plane strain is given by $\epsilon^m_{\alpha\beta} = \mathcal{M}^0(E\ \hat{\epsilon}_{\alpha\beta})$.

The moment is given by

$$M_{\alpha\beta} = \int_{-h/2}^{h/2} z\ \sigma^s_{\alpha\beta}(z)dz = \int_{-h/2}^{h/2} z\ E(z) f_{\alpha\beta\gamma\delta}(\kappa_{\gamma\delta}(z - z_0) + \epsilon_{\gamma\delta} - \hat{\epsilon}_{\gamma\delta}(z))dz$$
$$= f_{\alpha\beta\gamma\delta}(\kappa_{\gamma\delta}\left(\mathcal{M}^2(E) - z_0\mathcal{M}^1(E)\right) + \epsilon_{\gamma\delta}\mathcal{M}^1(E) - \mathcal{M}^1(E\ \hat{\epsilon}_{\gamma\delta}))$$
$$= f_{\alpha\beta\gamma\delta}\left(\kappa_{\gamma\delta}\left(\mathcal{M}^2(E) - \frac{\mathcal{M}^1(E)^2}{\mathcal{M}^0(E)}\right) + \epsilon_{\gamma\delta}\mathcal{M}^1(E) - \mathcal{M}^1(E\ \hat{\epsilon}_{\gamma\delta})\right).$$

Making the assumption that $\epsilon_{\gamma\delta} \approx \epsilon^m_{\gamma\delta}$, we have

$$= f_{\alpha\beta\gamma\delta}\left(\kappa_{\gamma\delta}\left(\mathcal{M}^2(E) - \frac{\mathcal{M}^1(E)^2}{\mathcal{M}^0(E)}\right) + \frac{\mathcal{M}^0\left(E\ \hat{\epsilon}_{\gamma\delta}\right)\mathcal{M}^1(E)}{\mathcal{M}^1(E)} - \mathcal{M}^1(E\ \hat{\epsilon}_{\gamma\delta})\right).$$

Defining $B = \mathcal{M}^2(E) - \frac{\mathcal{M}^1(E)^2}{\mathcal{M}^0(E)}$ and $\kappa^m_{\gamma\delta} = \frac{1}{B}\left(\mathcal{M}^1\left(E\ \hat{\epsilon}_{\gamma\delta}\right) - \frac{\mathcal{M}^1(E)\mathcal{M}^0\left(E\ \hat{\epsilon}_{\gamma\delta}\right)}{\mathcal{M}^0(E)}\right)$, we have

$$M_{\alpha\beta} = B\ f_{\alpha\beta\gamma\delta}\left(\kappa_{\gamma\delta} - \kappa^m_{\gamma\delta}\right).$$

These results allowed for calculation of the evolution of natural in-plane and bending strain relative to modulus as described in Table 2. Given the relations between strains, stresses, and curvatures, a Föppl-von Kármán energy was constructed of the form

$$\mathcal{E} = \int_\Omega \left(C\ W(\boldsymbol{\epsilon} - \boldsymbol{\epsilon}_m) + B\ W(\boldsymbol{\kappa} - \boldsymbol{\kappa}_m)\right)dA$$

where $\epsilon = \frac{1}{2}(\nabla \boldsymbol{u}(x) + \nabla \boldsymbol{u}(x)^T) + \frac{1}{2}\nabla w(x) \otimes \nabla w(x)$, $\boldsymbol{\kappa} = \nabla^2 w(x)$, and $C$, $B$, $\boldsymbol{\epsilon}_m$, $\boldsymbol{\kappa}_m$ are defined as in previous work. In this formulation, $\boldsymbol{u}(x) \in \mathbb{R}^2$ is the in-plane deformation of the neutral plane and $w(x) \in \mathbb{R}$ is the out of plane deformation. $W$ is the normalized strain energy function consistent with the plane stress approximation. Here, $W$ is defined as

$$W(\epsilon) = \frac{1}{2(1 - \nu^2)}\left(\nu\epsilon_{\alpha\alpha}\ \epsilon_{\beta\beta} + (1 - \nu)\epsilon_{\alpha\beta}\epsilon_{\alpha\beta}\right).$$

<u>Uniform Case</u>

As a demonstration of the consistency of the model, the case was considered where there are zero thermal stresses ($\hat{\epsilon}_{\alpha\beta}(z) = 0$) and the Young's Modulus is constant $E(z) = E$. We then have that $C = hE$, $B = \frac{h^3}{12}E$, $\epsilon_m = 0$, and $\kappa_m = 0$. The previous equation condenses to the standard Föppl-von Kármán plate energy of

$$\mathcal{E}_{FvK} = \int_\Omega \left(h\ E\ W\left(\frac{1}{2}(\nabla \boldsymbol{u}(x) + \nabla \boldsymbol{u}(x)^T) + \frac{1}{2}\nabla w(x) \otimes \nabla w(x)\right) + \frac{h^3 E}{12} W(\nabla^2 w(x))\right) dA.$$

Non-Dimensionalization

We then non-dimensionalized the problem. Letting $L$ be a characteristic macroscopic length scale (i.e. the side length of the sample), we then have

$$\bar{h} = \frac{h}{L}, \quad \bar{x} = \frac{x}{L}, \quad \bar{\boldsymbol{u}} = \frac{\boldsymbol{u}}{L}, \quad \bar{w} = \frac{w}{L}, \quad \bar{\Omega} = \frac{\Omega}{L^2}.$$

Using the chain rule on the gradients, the result is

$$\nabla \boldsymbol{u} = \nabla(L\,\bar{\boldsymbol{u}}) = \bar{\nabla}\bar{\boldsymbol{u}},$$
$$\nabla w = \nabla(L\,\bar{w}) = \bar{\nabla}\bar{w},$$
$$\nabla^2 w = \nabla(\bar{\nabla}\bar{w}) = \frac{1}{L}\bar{\nabla}^2\bar{w}$$

where $\bar{\nabla}$ is the gradient with respect to the non-dimensionalized coordinates $\bar{x}$. Plugging this in, $\mathcal{E}$ can be written as

$$\mathcal{E} = \int_{\Omega} (C\,W(\boldsymbol{\epsilon} - \boldsymbol{\epsilon}_m) + B\,W(\boldsymbol{\kappa} - \boldsymbol{\kappa}_m))dA$$
$$= \int_{\bar{\Omega}} \left( C\,W(\bar{\boldsymbol{\epsilon}} - \boldsymbol{\epsilon}_m) + B\,W\left(\frac{1}{L}\bar{\boldsymbol{\kappa}} - \boldsymbol{\kappa}_m\right)\right) L^2\,d\bar{A}$$

where $\bar{\boldsymbol{\epsilon}} = \frac{1}{2}(\bar{\nabla}\bar{\boldsymbol{u}} + \bar{\nabla}\bar{\boldsymbol{u}}^T) + \frac{1}{2}\bar{\nabla}\bar{w} \otimes \bar{\nabla}\bar{w}$ and $\bar{\boldsymbol{\kappa}} = \bar{\nabla}^2\bar{w}$. Because $W$ is a quadratic form, $W(\alpha \boldsymbol{F}) = \alpha^2 W(\boldsymbol{F})$ for all $\alpha \in \mathbb{R}$. Defining $\bar{\boldsymbol{\kappa}}_m = L\,\boldsymbol{\kappa}_m$, the result is

$$\mathcal{E} = \int_{\bar{\Omega}} \left( C\,W(\bar{\boldsymbol{\epsilon}} - \boldsymbol{\epsilon}_m) + \frac{B}{L^2} W(\bar{\boldsymbol{\kappa}} - \bar{\boldsymbol{\kappa}}_m)\right) L^2 d\bar{A}$$
$$= L^2 C \int_{\bar{\Omega}} \left( W(\bar{\boldsymbol{\epsilon}} - \boldsymbol{\epsilon}_m) + \frac{B}{CL^2} W(\bar{\boldsymbol{\kappa}} - \bar{\boldsymbol{\kappa}}_m)\right) d\bar{A}.$$

This allowed for rescaling of the problem to a unit scale for numerical stability. Additionally, we obtained a non-dimensionalized form of the energy as

$$\bar{\mathcal{E}} = \frac{\mathcal{E}}{L^2 C} = \int_{\bar{\Omega}} \left( W(\bar{\boldsymbol{\epsilon}} - \boldsymbol{\epsilon}_m) + \bar{B} W(\bar{\boldsymbol{\kappa}} - \bar{\boldsymbol{\kappa}}_m)\right) d\bar{A} \tag{1}$$

where $\bar{B} = \frac{B}{CL^2}$ is the normalized bending modulus. Minimizing this elastic energy yields equilibrium solutions. But first, temperature distribution through the thickness needed to be obtained.

Heat Equation and Boundary Conditions

The temperature distribution through the thickness was obtained and its evolution over time was defined by solving following heat equation and boundary conditions.

$$\frac{\partial T}{\partial t}(z,t) = D\frac{\partial^2 T}{\partial z^2}(z,t)$$
$$T\left(-\frac{h}{2}, t\right) = T_l$$
$$\frac{\partial T}{\partial z}\left(\frac{h}{2}, t\right) = 0$$
$$T(z,0) = T_0$$

The above system was solved using the pdepe routine in Matlab to obtain $T(z,t)$. This result was used in combination with the strain as a function of temperature for different combinations of laminated films. For example, with two laminated films (both of height h/2), the result is

$$\epsilon_{\alpha\beta}(\Delta T, z) = \begin{cases} \epsilon^1_{\alpha\beta}(\Delta T), & z \in (0, h/2) \\ \epsilon^2_{\alpha\beta}(\Delta T), & z \in (-h/2, 0) \end{cases}$$

where $\epsilon^1_{\alpha\beta}(\Delta T)$ and $\epsilon^2_{\alpha\beta}(\Delta T)$ are the (experimentally measured) strain functions for each of the individual laminates. For any given time, we can find the spontaneous strain through the thickness as

$$\hat{\epsilon}_{\alpha\beta}(z) = \epsilon_{\alpha\beta}(T(z,t) - T_0, z)$$

where the explicit dependence on $t$ is suppressed. Note that this term also encapsulates the radial nature of the patterning on the LCE sheet.

Equilibrium shape

Having obtained the temperature distribution and the resulting spontaneous stretch and curvature, we sought to study the equilibria associated with the energy (1) to obtain the shape of the sheet. This was non-trivial due to the presence of the second derivative ($\nabla\nabla w$); so, an augmented Lagrangian method was used. The strain energy (1) is written compactly as

$$U_{vK}[\boldsymbol{u}, w] = \int_\Omega u_{vK}(\boldsymbol{u}, \nabla\boldsymbol{u}, w, \nabla w, \nabla\nabla w) da.$$

A new function, $\boldsymbol{\xi}$ , was then introduced which we constrain as $\boldsymbol{\xi} = \nabla w$. This constraint was enforced with an augmented Lagrangian written as

$$\mathcal{L}_{vK}[\boldsymbol{u}, w, \boldsymbol{\xi}, \boldsymbol{\lambda}] = \int_\Omega u_{vK}(\boldsymbol{u}, \nabla\boldsymbol{u}, w, \nabla w, \nabla\boldsymbol{\xi}) da - \int_\Omega \boldsymbol{\lambda} \cdot (\boldsymbol{\xi} - \nabla w) da + \frac{\mu}{2} \int_\Omega |\boldsymbol{\xi} - \nabla w|^2 da$$

where the contribution of the Lagrange multiplier $\boldsymbol{\lambda}$ must also be solved for. The weak form of this Lagrangian is found by taking variations and solving for $\delta\mathcal{L}[\boldsymbol{u}, w, \boldsymbol{\xi}, \boldsymbol{\lambda}] = 0$. This is similar to the approach of "mixed elements" in the Mindlin-Reissner plate theory, as described in (*36*) with an added quadratic relaxation term in the energy. Following the standard finite element formulation, we expanded both the function and its corresponding variation with Galerkin projections as

$$\boldsymbol{u}^p(x) = \sum \boldsymbol{u}^i N_i^u(\boldsymbol{x}), \quad w^p(\boldsymbol{x}) = \sum w^i N_i^w(\boldsymbol{x}), \quad \boldsymbol{\lambda}^p(x) = \sum \boldsymbol{\lambda}^i N_i^\lambda(\boldsymbol{x}), \quad \boldsymbol{\xi}^p(\boldsymbol{x}) = \sum \boldsymbol{\xi}^i N_i^\xi(\boldsymbol{x})$$

where $N_i^{(\cdot)}$ are the shape functions with compact support. 2nd order shape functions were used in $\boldsymbol{u}$ and first order for all the rest. The finite element scheme was implemented in Deal.II, a finite element library for C++. (*37*) The zero was found using Newton-Raphson iterations where the Hessian is found using the second variation of the augmented Lagrangian.

Calculating Critical Curvatures

We started at the flat shape when the temperature distribution is uniform. At each subsequent time step, the temperature distribution was computed and used to obtain the spontaneous strain and curvature distributions. These were then used compute the new equilibrium shape using the previous shape as an initial guess, which led to a smooth evolution until system lost stability. The loss of stability is seen when the Newton-Raphson iteration fails to converge or when the solution jumps significantly. The shape of the snapped configuration was then calculated. This

method provided the verification and demonstration of snap-through as seen in Figure 2E. In order to calculate the relationship between a particular fixed value of in-plane strain and the spontaneous curvature necessary to cause inversion, the configuration for that fixed value of in-plane strain was calculated in the absence of any spontaneous curvature. The inverting curvature then slowly increased, again leading to smooth deformations, until the Newton-Raphson iteration fails to converge or the solution jumps significantly. At this point, shape of the snapped configuration was calculated and the critical curvature necessary for inversion was calculated as well as the difference in stored strain energies before and after the snap-through. By repeating this process for various values of in-plane strain, the relationship between in-plane strain and the critical curvature necessary for inversion was able to be calculated. This method was used for calculating the results in Figures 3B,C and 4A,B.

Jump Height

To estimate of the height that the sheet will jump off the table, it was assumed that all of the energy released in the snap-through was converted to gravitational potential energy. Calculated in the non-dimensional scheme, the snap-through releases some $\Delta\bar{\mathcal{E}}$. This was converted to a dimensional energy as $\Delta\mathcal{E} = L^2 C\, \Delta\bar{\mathcal{E}}$, with non-dimensionalization done as described above. We then equated the released energy to the gravitational potential energy as

$$\Delta\mathcal{E} = m\, g\, \hat{z}$$

where $\hat{z}$ is the estimated jump height. Rearranging, the result is

$$\hat{z} = \frac{L^2 C}{L^2 h \rho g}\Delta\bar{\mathcal{E}} = \frac{C}{\rho g h}\Delta\bar{\mathcal{E}}$$

where we take $m = \rho L^2 h$ and use the values denoted in Table S1 for analysis.

**Table S1. Values assigned to variables in computational analysis of jump height.**

| Variable | Value |
|---|---|
| $C$ | $1.053 * 10^3\ m\ Pa$ |
| $h$ | $90\ \mu m$ |
| $\rho$ | $1.2\ g/cm^3$ |
| $g$ | $9.8\ m/s^2$ |
| $\Delta\bar{\mathcal{E}}$ | $2.0 * 10^{-4}$ |

Substituting values from the simulations, the result was $\hat{z} \approx 20\ cm$. Interestingly, it seems that regardless of the dimension of the system, the jump height is the same. This qualitatively matched the behavior of the experimental system. Note that in reality, there are dissipative processes that reduce the jump height. Some of these include dissipation within the material, non-ideal heat transfer, liftoff, and kinetic energy from non-rigid body effects; therefore, this solution should be considered an upper bound on the jump height.

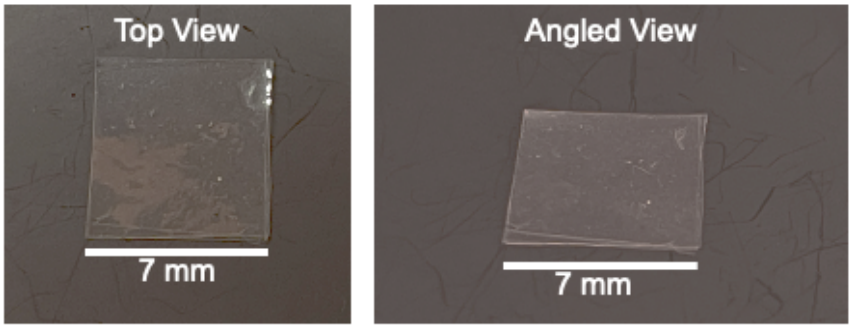


**Figure S1**. **Starting from a flat state.** Images of the LCE element in the flat state before heating

**Movie S1.**
Leaping of laminated liquid crystalline elastomer. Material is placed with the high-modulus side in contact with the hot plate at 160 °C.

**Movie S2.**
Laminated liquid crystalline elastomer placed with the low-modulus side in contact with the hot plate at 160 °C, showing no snap-through behavior.

**Movie S3.**
Laminated liquid crystalline elastomer with defect center at fractional offset of 0.1. Material is placed with the high-modulus side in contact with the hot plate at 160 °C.

**Movie S4.**
Laminated liquid crystalline elastomer with defect center at fractional offset of 0.2. Material is placed with the high-modulus side in contact with the hot plate at 160 °C.

**Movie S5.**
Laminated liquid crystalline elastomer with defect center at fractional offset of 0.3. Material is placed with the high-modulus side in contact with the hot plate at 160 °C.

**Movie S6.**
Laminated liquid crystalline elastomer with two high modulus layers and one low modulus layer. Material is placed with the high-modulus side in contact with the hot plate at 160 °C.

**Movie S7.**
Laminated liquid crystalline elastomer with one high modulus layer and one low modulus layer. Material is placed with the high-modulus side in contact with the hot plate at 160 °C.

**Movie S8.**
Laminated liquid crystalline elastomer with one high modulus layer and three low modulus layers. Material is placed with the high-modulus side in contact with the hot plate at 160 °C.

**Movie S9.**
Directional leaping of laminated liquid crystalline elastomer with leg lengths of 0.5 mm and 1 mm. Material is placed with the high-modulus side in contact with the hot plate at 160 °C.

**Movie S10.**
Actuation of laminated liquid crystalline elastomer with leg lengths of 1.5 mm and 1.5 mm. Material is placed with the high-modulus side in contact with the hot plate at 160 °C.

**Movie S11**.
Actuation of laminated liquid crystalline elastomer with leg lengths of 0 mm and 1.5 mm. Material is placed with the high-modulus side in contact with the hot plate at 160 °C.

**Movie S12.**
Actuation of laminated liquid crystalline elastomer with leg lengths of 0.5 mm and 1.5 mm. Material is placed with the high-modulus side in contact with the hot plate at 160 °C.

**Movie S13.**
Demonstration of repeated actuation over 9 cycles. Material is placed with the high-modulus side in contact with the hot plate at 160 °C and cooled between cycles to room temperature.

**Movie S14.**
Leaping of LCE laminate fabricated with a circular perimeter. Material is placed with the high-modulus side in contact with the hot plate at 160 °C.

## REFERENCES


1. M. Pilz da Cunha, S. Ambergen, M. G. Debije, E. F. G. A. Homburg, J. M. J. den Toonder, A. P. H. J. Schenning, A soft transporter robot fueled by light. *Adv. Sci.* **7**, 1902846 (2020).

2. S. Chen, Y. Cao, M. Sarparast, H. Yuan, L. Dong, X. Tan, C. Cao, Soft crawling robots: Design, actuation, and locomotion. *Adv. Mater. Technol.* **5**, 1900837 (2020).

3. Z. Liu, R. Zhang, Y. Xiao, J. Li, W. Chang, D. Qian, Z. Liu, Somatosensitive film soft crawling robots driven by artificial muscle for load carrying and multi-terrain locomotion. *Mater Horiz.* **8**, 1783–1794 (2021).

4. S. Gantenbein, K. Masania, W. Woigk, J. P. W. Sesseg, T. A. Tervoort, A. R. Studart, Three-dimensional printing of hierarchical liquid-crystal-polymer structures. *Nature* **561**, 226–230 (2018).

5. M. P. da Cunha, M. G. Debije, A. P. H. J. Schenning, Bioinspired light-driven soft robots based on liquid crystal polymers. *Chem. Soc. Rev.* **49**, 6568–6578 (2020).

6. E. Queathem, The ontogeny of grasshopper jumping performance. *J. Insect Physiol.* **37**, 129–138 (1991).

7. H. C. Astley, T. J. Roberts, Evidence for a vertebrate catapult: Elastic energy storage in the plantaris tendon during frog jumping. *Biol. Lett.* **8**, 386–389 (2012).

8. H. C. Astley, T. J. Roberts, The mechanics of elastic loading and recoil in anuran jumping. *J. Exp. Biol.* **217**, 4372–4378 (2014).

9. M. J. Schwaner, D. C. Lin, C. P. McGowan, Jumping mechanics of desert kangaroo rats. *J. Exp. Biol.* **221**, jeb186700 (2018).

10. M. Gomez, D. E. Moulton, D. Vella, Dynamics of viscoelastic snap-through. *J. Mech. Phys. Solids* **124**, 781–813 (2019).

11. Y. Kim, J. van den Berg, A. J. Crosby, Autonomous snapping and jumping polymer gels. *Nat. Mater.* **20**, 1695–1701 (2021).

12. J. Jeon, J. C. Choi, H. Lee, W. Cho, K. Lee, J. G. Kim, J. W. Lee, K. Il Joo, M. Cho, H. R. Kim, J. J. Wie, Continuous and programmable photomechanical jumping of polymer monoliths. *Mater. Today*, **49**, 97–106 (2021).

13. K. Korner, A. S. Kuenstler, R. C. Hayward, B. Audoly, K. Bhattacharya, A nonlinear beam model of photomotile structures. *Proc. Natl. Acad. Sci. U.S.A.* **117**, 9762–9770 (2020).

14. H. Arazoe, D. Miyajima, K. Akaike, F. Araoka, E. Sato, T. Hikima, M. Kawamoto, T. Aida, An autonomous actuator driven by fluctuations in ambient humidity. *Nat. Mater.* **15**, 1084–1089 (2016).

15. B. Gorissen, D. Melancon, N. Vasios, M. Torbati, K. Bertoldi, Inflatable soft jumper inspired by shell snapping. *Sci Robot.* **5**, eabb1967 (2020).

16. T. J. White, D. J. Broer, Programmable and adaptive mechanics with liquid crystal polymer networks and elastomers. *Nat. Mater.* **14**, 1087–1098 (2015).

17. J. Küpfer, H. Finkelmann, Nematic liquid single crystal elastomers. *Die Makromol. Chem. Rapid Commun.* **12**, 717–726 (1991).

18. G. N. Mol, K. D. Harris, C. W. M. Bastiaansen, D. J. Broer, Thermo-mechanical responses of liquid-crystal networks with a splayed molecular organization. *Adv. Funct. Mater.* **15**, 1155–1159 (2005).

19. K. Fuchi, T. H. Ware, P. R. Buskohl, G. W. Reich, R. A. Vaia, T. J. White, J. J. Joo, Topology optimization for the design of folding liquid crystal elastomer actuators. *Soft Matter* **11**, 7288–7295 (2015).

20. B. A. Kowalski, C. Mostajeran, N. P. Godman, M. Warner, T. J. White, Curvature by design and on demand in liquid crystal elastomers. *Phys Rev E* **97**, 012504 (2018).

21. T. Guin, M. J. Settle, B. A. Kowalski, A. D. Auguste, R. V. Beblo, G. W. Reich, T. J. White, Layered liquid crystal elastomer actuators. *Nat. Commun.* **9**, 2531 (2018).

22. M. Pilz da Cunha, Y. Foelen, R. J. H. Raak, J. N. Murphy, T. A. P. Engels, M. G. Debije, A. P. H. J. Schenning, Liquid crystal soft robot: An untethered magnetic- and light-responsive rotary gripper: Shedding light on photoresponsive liquid crystal actuators (Advanced Optical Materials 7/2019). *Adv Opt Mater.* **7**, 1970025 (2019).

23. A. Lebar, G. Cordoyiannis, Z. Kutnjak, B. Zalar, The isotropic-to-nematic conversion in liquid crystalline elastomers, in *Liquid Crystal Elastomers: Materials and Applications*, W. de Jeu, Ed. (Springer, 2010).

24. M. Ravi Shankar, M. L. Smith, V. P. Tondiglia, K. M. Lee, M. E. McConney, D. H. Wang, L. S. Tan, T. J. White, Contactless, photoinitiated snap-through in azobenzene-functionalized polymers. *Proc. Natl. Acad. Sci. U.S.A.* **110**, 18792–18797 (2013).

25. C. P. Ambulo, J. J. Burroughs, J. M. Boothby, H. Kim, M. R. Shankar, T. H. Ware, Four-dimensional printing of liquid crystal elastomers. *ACS Appl. Mater. Interfaces* **9**, 37332–37339 (2017).

26. M. Li, S. Lv, J. Zhou, Photo-thermo-mechanically actuated bending and snapping kinetics of liquid crystal elastomer cantilever. *Smart Mater Struct.* **23**, 125012 (2014).

27. D. Ge, K. Li, Pulsating self-snapping of a liquid crystal elastomer bilayer spherical shell under steady illumination. *Int. J. Mech. Sci.* **233**, 107646 (2022).

28. T. H. Ware, M. E. McConney, J. J. Wie, V. P. Tondiglia, T. J. White, Voxelated liquid crystal elastomers. *Science* **347**, 982–984 (2015).

29. S. Ahn, T. H. Ware, K. M. Lee, V. P. Tondiglia, T. J. White, Photoinduced topographical feature development in blueprinted azobenzene-functionalized liquid crystalline elastomers. *Adv. Funct. Mater.* **26**, 5819–5826 (2016).

30. M. Warner, Topographic mechanics and applications of liquid crystalline solids. *Annu. Rev. Condens. Matter Phys.* **11**, 125–145 (2020).

31. L. T. de Haan, C. Sánchez-Somolinos, C. M. W. Bastiaansen, A. P. H. J. Schenning, D. J. Broer, Engineering of complex order and the macroscopic deformation of liquid crystal polymer networks. *Angew. Chem. Int. Ed. Engl.* **51**, 12469–12472 (2012).

32. T. S. Hebner, H. E. Fowler, K. M. Herbert, N. P. Skillin, C. N. Bowman, T. J. White, Polymer network structure, properties, and formation of liquid crystalline elastomers prepared via thiol–acrylate chain transfer reactions. *Macromolecules* **54**, 11074–11082 (2021).

33. C. D. Modes, K. Bhattacharya, M. Warner, Gaussian curvature from flat elastica sheets. *Proc. R. Soc. A* **467**, 1121–1140 (2011).

34. M. Pezzulla, N. Stoop, M. P. Steranka, A. J. Bade, D. P. Holmes, Curvature-induced instabilities of shells. *Phys. Rev. Lett.* **120**, 048002 (2018).

35. M. Taffetani, X. Jiang, D. P. Holmes, D. Vella, Static bistability of spherical caps. *Proc. R. Soc. A* **474**, 20170910 (2018).

36. O. C. Zienkiewicz, R. L. Taylor, *The Finite Element Method: Solid Mechanics* (Butterworth-Heinemann, 2000), vol. 2.

37. D. Arndt, W. Bangerth, B. Blais, M. Fehling, R. Gassmöller, T. Heister, L. Heltai, U. Köcher, M. Kronbichler, M. Maier, P. Munch, J. P. Pelteret, S. Proell, K. Simon, B. Turcksin, D. Wells, J. Zhang, The deal.II library, version 9.3. *J. Num. Math.* **29**, 171–186 (2021).